Applied Surface Science 462 (2018) 344–352

Contents lists available at ScienceDirect

Applied Surface Science

journal homepage: www.elsevier.com/locate/apsusc

Full Length Article

Surface chemistry and the corrosion behavior of magnetron sputtered niobium oxide films in sulfuric acid solution

Marina Fuser Pillis[a], Mara Cristina Lopes de Oliveira[b], Renato Altobelli Antunes[b,*]

[a] Instituto de Pesquisas Energéticas e Nucleares (IPEN/CNEN-SP), Centro de Ciência e Tecnologia de Materiais (CCTM), 05508-000 São Paulo, SP, Brazil
[b] Centro de Engenharia, Modelagem e Ciências Sociais Aplicadas (CECS), Universidade Federal do ABC (UFABC), 09210-580 Santo André, SP, Brazil

ARTICLE INFO

Keywords:
Nb_2O_5 films
Magnetron sputtering
XPS
Corrosion
Sulfuric acid solution

ABSTRACT

In this work, magnetron sputtered Nb_2O_5 films were obtained at two different deposition times. The surface chemistry of the deposited layers was investigated by X-ray photoelectron spectroscopy (XPS). The corrosion behavior was assessed by electrochemical impedance spectroscopy, potentiodynamic polarization and potentiostatic polarization tests in 0.5 M H_2SO_4 + 2 ppm HF solution at room temperature. The Nb^{5+}/Nb^{4+} ratio decreased with the deposition time, leading to a higher surface activity for the film obtained at 30 min. This result was confirmed by its lower impedance values and higher current densities when compared to the 15′-film. Surface chemistry played a major role on the corrosion behavior of the sputtered films and can be tailored by the deposition time.

1. Introduction

Stainless steels have been considered as potential candidates for bipolar plates of polymer electrolyte membrane fuel cells (PEMFC) due to a combination of good formability at a low cost and mechanical stability [1–3]. Long-term exposure to the acidic environment of PEMFCs, though, can deteriorate the performance of stainless steel bipolar plates due to corrosion [4,5]. Corrosion processes can increase the surface electrical resistivity as a consequence of the formation of a low-conductivity oxide film [6]. In addition, corrosion can release metallic ions that poison the catalyst layer on the polymer electrolyte membrane, thus reducing the fuel cell electrical efficiency [7,8].

One interesting route to avoid the above-mentioned corrosion concerns is by applying protective coatings on the stainless steel surface [9–11]. A variety of materials and processes have been employed for protecting stainless steel bipolar plates from corrosion in the PEMFC environment such as metal nitrides and carbides obtained by physical vapor deposition processes [12–16]. Recently, niobium-based compounds have attracted attention as corrosion resistant thin films for stainless steels, low alloy steels, magnesium alloys and aluminum substrates [17–20].

Niobium oxides play a core role in this scenario as they are intrinsically resistant to corrosion [21,22]. Niobium pentoxide (Nb_2O_5) thin films, in particular, are envisaged as promising protective coatings. It is the most thermodynamically stable niobium oxide species [23]. It presents a set of engineering attributes such as high wear resistance, biocompatibility, thermal stability and high photoelectric and photocatalytic activities, making it attractive for a variety of applications in the biomedical and electronic fields [24,25]. Good corrosion properties have been reported in conventional sodium chloride solutions [26,27].

Additionally, the suitability of Nb_2O_5 films to protect stainless steels against corrosion in the acidic environment of PEMFCs has been exploited by some authors. Pan et al. [28] have employed high energy micro arc alloying technique (HEMAA) to obtain Nb_2O_5 films on AISI 304 stainless steel substrates. The corrosion resistance of the coated steel was assessed in a typical PEMFC environment. The Nb_2O_5 film increased the steel chemical stability. Cao et al. [29] reported the high chemical inertness of Nb_2O_5 layer formed on the surface of an electrodeposited niobium film deposited on 316 stainless steel substrates after exposure to typical acid solution of PEMFCs.

In spite of the reports mentioned above, to the best of the authors' knowledge there is no information in the current literature exploring the correlation between the surface chemistry and the corrosion behavior of Nb_2O_5 films in typical PEMFC environment. In this respect, the aim of the present work was to investigate the effect of deposition time on the corrosion behavior of Nb_2O_5-coated 316 stainless steel specimens in 0.5 M H_2SO_4 + 2 ppm HF solution. The films were deposited by magnetron sputtering. Surface chemistry was assessed by X-ray photoelectron spectroscopy (XPS).

* Corresponding author.
E-mail address: renato.antunes@ufabc.edu.br (R.A. Antunes).

https://doi.org/10.1016/j.apsusc.2018.08.123
Received 14 April 2018; Received in revised form 14 August 2018; Accepted 16 August 2018
Available online 17 August 2018
0169-4332/

2. Materials and methods

2.1. Film deposition

The first step for film deposition was substrate preparation. AISI 316 circular pieces were employed as substrates (19 mm-diameter and 6 mm-thickness). Surface finishing was carried out by grinding with SiC waterproof paper up to grit 600. Next, the samples were degreased with acetone and washed with distilled water, following drying in nitrogen flux. These samples were employed for the electrochemical measurements. Silicon (1 0 0) wafers were used as substrates for characterization by ellipsometry.

DC (direct current) magnetron sputtering was used to obtain the Nb_2O_5 layers. The deposition process was carried out at room temperature under $Ar + O_2$ atmosphere. Ar and O_2 flows were 100 mL·min^{-1} and 15 mL·min^{-1}, respectively. The niobium source was a 99.9% purity niobium target. The substrate was located at a distance of 15 cm from the target. Two different deposition times were tested: 15 and 30 min. The chamber pressure was held constant at 0.084 Pa. The DC power was 400 W. In a previous report [27], our group has shown that the films obtained by this procedure are compact but present surface porosity that increases with the deposition time.

2.2. Film characterization

Film thickness was determined using ellipsometry. The measurements were performed using a Rudolph Research Corporation ellipsometer, model Auto EL IV MS with incident angle of 70° and wavelength of 632.8 nm. The thicknesses were 36 nm and 70 nm for the films obtained at the deposition times of 15′ and 30′, respectively.

XPS measurements were carried out to investigate the chemical states of niobium and oxygen at the surface of the AISI 316 substrate. The spectra were acquired using a Thermo Scienctific K-Alpha$^+$ spectrometer with a monochromated Al-Kα X-ray source and calibrated to the adventitious C1s peak at 284.8 eV. Chemical state assessment was achieved by curve-fitting the spectra using the Avantage^{TM} software. Depth profile experiments were also carried out by sputtering the surface of the niobium-coated samples with Ar^+ ions. Each sputtering cycle consisted of 30 s Ar^+ etching with energy of 3 keV.

The corrosion resistance was evaluated by electrochemical impedance spectroscopy (EIS) measurements, potentiostatic and potentiodynamic polarization tests. The test solution was comprised of 0.5 M H_2SO_4 + 2 ppm HF at room temperature. The samples remained immersed for 1 h in the electrolyte. The EIS measurements were performed in the frequency range from 100 kHz to 10 mHz with an amplitude of the perturbation signal of ± 10 mV (rms) and an acquisition rate of 10 points per decade at the open circuit potential. Right after the EIS measurements, potentiodynamic polarization tests were performed from −300 mV versus the OCP up to 1000 mV at a rate of 1 mV·s^{-1}. Potentiostatic polarization tests were carried out in a second set of experiments using the same electrolyte described above. The samples were polarized at −0.1 $V_{Ag/AgCl}$ and + 0.6 $V_{Ag/AgCl}$ for 1 h. The variation of the current density with time was continuously monitored during the potentiostatic tests. The tests were conducted in triplicate.

3. Results

3.1. XPS analysis

3.1.1. Survey spectra

Fig. 1 shows the XPS survey spectra of the niobium-coated AISI 316 specimens. The main components were quantified and the results are shown in Table 1.

The Nb3d peak becomes more intense as the deposition time increases. Peaks from the substrate (Fe2p, Cr2p and Ni2p) were also detected for the 15′-film. However, they were not found for the 30′ film, indicating that the niobium-layer became thicker for this condition, as determined by ellipsometry.

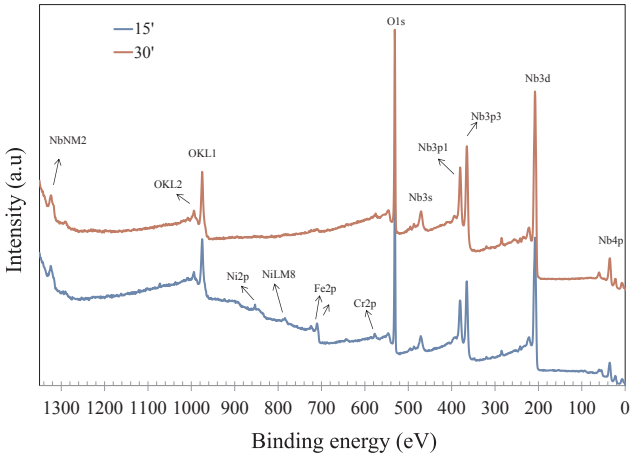

Fig. 1. XPS survey spectra of the niobium-coated AISI 316 stainless steel specimens.

Table 1
Atomic concentrations of Nb3d, O1s, Fe2p, Cr2p and Ni2p determined from the XPS survey spectra.

Deposition time (min)	Nb3d (at. %)	O1s (at. %)	Fe2p (at. %)	Cr2p (at. %)	Ni2p (at. %)
15′	25.11	67.70	6.01	0.37	0.83
30′	31.15	68.85	–	–	–

3.1.2. Core levels

The chemical states of niobium and oxygen were determined by XPS analyses. Fig. 2 shows the Nb 3d core levels for the niobium-based films obtained at different deposition times. Table 2 displays the atomic concentrations of different components as obtained from the fitting procedure of the Nb3d core levels spectra. Niobium was found at two different oxidation states Nb^{4+} and Nb^{5+}. The Nb^{5+}/Nb^{4+} ratio is also displayed in Table 2. Fig. 3 shows the O1s core levels for the niobium-based films. The atomic concentrations of the oxygen components are shown in Table 3.

Peak fitting of the Nb3d spectra at the surface of the different films revealed that niobium exists at two different oxidation states in the as-deposited films, Nb^{4+} (NbO_2) and Nb^{5+} (Nb_2O_5). The spectra show two doublets for $Nb3d_{5/2}$ and $Nb3d_{3/2}$ either for the Nb^{5+} or Nb^{4+} species. The binding energies at which each component is centered are indicated in Table 2 and are in agreement with the literature [30–33]. The Nb_2O_5 component predominates over the NbO_2 component. The Nb^{5+}/Nb^{4+} ratio decreases with the deposition time, indicating that the film became enriched in the NbO_2 component for longer times. Notwithstanding, the Nb_2O_5 atomic concentration greatly surpasses that of NbO_2 for both deposition times. The occurrence of the Nb^{4+} oxidation state in the Nb_2O_5 structure has been reported by Li et al. [34] and was attributed to the formation of oxygen vacancies during formation of the Nb_2O_5 compound.

The O1s core levels were deconvoluted into two components for both deposition times. The first component at lower binding energies is assigned to the oxygen in the oxygen-metal-oxygen bond and corresponding to O^{2-} anions [35]. The higher binding energy component is assigned to oxygen in the metal-OH bond or adsorbed water molecules [36]. It is seen from Table 3 that O^{2-} is the main component for all films and its atomic concentration slightly decreases with the deposition time.

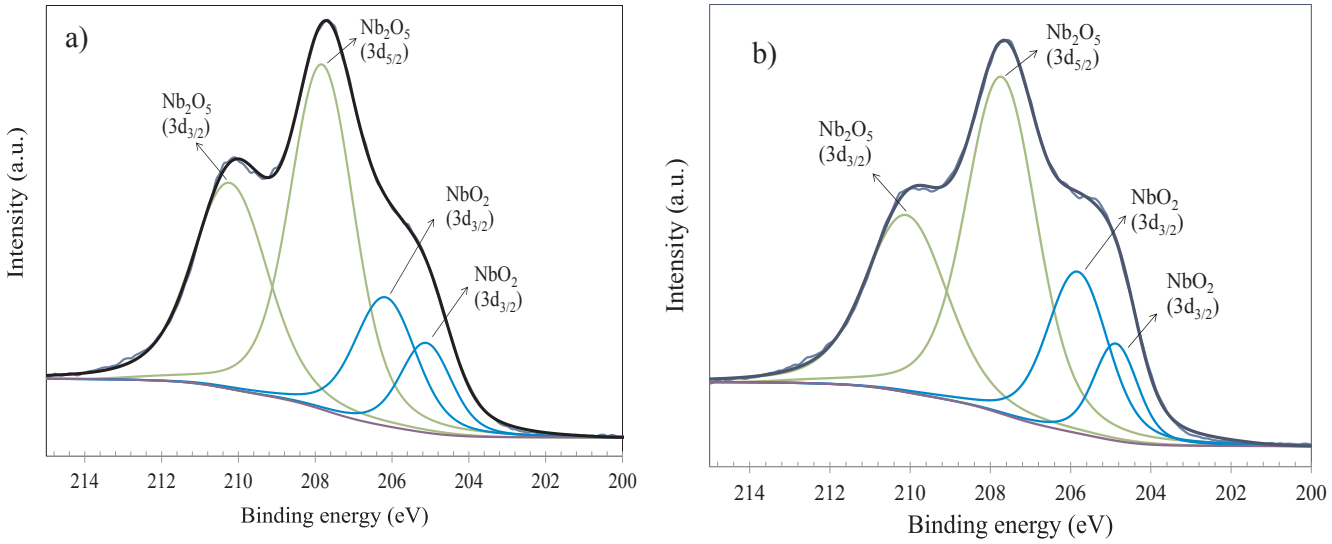

Fig. 2. Nb3d core levels for the niobium-based films obtained from the surface of the AISI 316 stainless steel specimens at different deposition times: (a) 15 min; (b) 30 min.

3.1.3. Depth profile

XPS depth profile experiments of the niobium-coated AISI 316 specimens were performed to study the atomic concentrations of the main elements in the niobium-based films after sputtering with Ar^+ ions. Fig. 4 shows the variation of the atomic concentrations of Nb3d, O1s, Fe2p and Cr2p with sputtering time for the different films. The depth profiles reveal that Nb3d atomic concentration is more rapidly decreased with the etch time for the 15′ condition. For the 30‘ it remained almost unchanged up to the third etching cycle (30 s) and then started to decrease slowly up to the end of the test. It reached 6.61 at.% after 140 s whereas it was very lower for the 15′-film for the same time (0.77 at.%). The variations of Fe2p and Cr2p atomic concentrations are opposite with respect to that of Nb3d. As the Nb3d concentration decreases the Fe2p and Cr2p fractions increase for all deposition times. There is, though, a significant difference between the rate with which the substrate components increase with the etch time. For the 15′-film the increase of Fe2p and Cr2p occurs steadily after 20 s and then reaches a plateau after 90 s, suggesting that the film is almost completely removed after this time. For the 30′-film the increase of Fe2p and Cr2p atomic concentrations starts after 40 s and does not reach a stable plateau as occurred for the 15′-condition. The variation of the O1s atomic concentration follows that of the Fe2p and Cr2p, being related to the thickness of the niobium-based layer. As the niobium-based film becomes thicker, the O1s fraction become more stable with the etch time.

3.2. Corrosion behavior

The variation of the open circuit potential versus time for the Nb_2O_5-coated AISI 316 stainless steel samples immersed in 0.5 M H_2SO_4 + 2 ppm HF solution at room temperature is shown in Fig. 5. The potential tends to gradually increase for all niobium-based films. This variation is typical of passive layers, being associated oxide film thickening with time [37]. The potential increases continuously with time, showing a stabilization trend. The same behavior is observed for the uncoated substrate.

Right after the 1 h-monitoring period EIS measurements were carried out at the open circuit potential. Fig. 6 shows Nyquist and Bode plots for the Nb_2O_5-coated AISI 316 stainless steel specimens in 0.5 M H_2SO_4 + 2 ppm HF solution at room temperature. The Nyquist plots (Fig. 6a) are characterized by capacitive loops that are flattened at the low frequency domain, indicating similar corrosion mechanism independently of the deposition time. Notwithstanding, some differences can be highlighted for the Nb_2O_5-coated samples with respect to their corrosion resistance. The diameter of the capacitive loop is associated with the polarization resistance of the electrode surface [38,39], scaling up with it. In this respect, the 15′-film presents the highest corrosion resistance, since its capacitive loop displays the largest diameter compared to the 30′.

Phase angle plots suggest the presence of one single time constant characterized by the presence of a well-defined peak at the intermediate frequency domain whose maximum value reaches −75° for all Nb_2O_5 films and the uncoated substrate. At lower frequencies, the phase angles sharply dropped off, suggesting the onset of corrosion processes [40]. The impedance modulus of the uncoated substrate was lower than that of the Nb_2O_5-coated specimens. The highest impedance modulus was for the 15′-film. The slope of the log |Z| vs. log f plot is equal to −1 only up to 1 Hz, denoting typical capacitive behavior. For lower frequencies, though, log |Z| is nearly parallel to the x-axis and the EIS response becomes independent on the applied frequency, indicating its resistive character and the loss of corrosion resistance [41].

Potentiodynamic polarization curves for the uncoated and Nb_2O_5-

Table 2
XPS fitting results for the high-resolution spectra of Nb3d core level.

Film/Component	15′			30′		
	BE (eV)	FWHM (eV)	at.%	BE (eV)	FWHM (eV)	at.%
Nb_2O_5 $3d_{5/2}$	207.72	1.97	43.94	207.62	2.09	45.55
Nb_2O_5 $3d_{3/2}$	210.13	2.34	31.13	210.00	2.41	27.61
NbO_2 $3d_{5/2}$	205.01	1.58	9.16	204.77	1.31	8.18
NbO_2 $3d_{3/2}$	206.07	1.90	15.76	205.73	1.79	18.66
Nb^{5+}/Nb^{4+}	3.01			2.73		

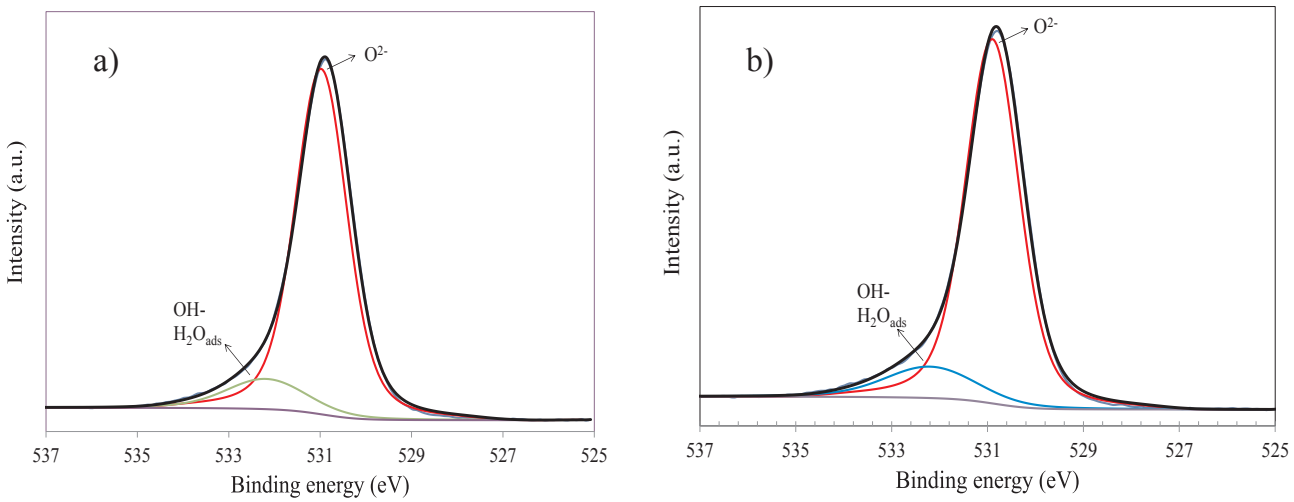

Fig. 3. O1s core levels for the niobium-based films obtained from the surface of the AISI 316 stainless steel specimens at different deposition times: (a) 15 min; (b) 30 min.

Table 3
XPS fitting results for the high-resolution spectra of O1s core level.

Component	15′		30′	
	O^{2-}	Adsorbed H_2O or OH^-	O^{2-}	Adsorbed H_2O or OH^-
BE (eV)	530.88	532.09	530.80	532.10
FWHM (eV)	1.34	2.06	1.33	2.23
at.%	88.13	11.87	87.38	12.62

coated AISI 316 stainless steel upon immersed in 0.5 M H_2SO_4 + 2 ppm HF solution at room temperature are shown in Fig. 7. Horizontal lines indicating the typical operating potentials of PEM fuel cells at the anode (−0.1 V) and cathode (+0.6 V) sides are also marked in this figure and can be used as guidelines to correlate the electrochemical behavior of the different samples with a more actual PEMFC environment. Values of corrosion potential (E_{corr}), Flade potential (E_{Flade}), passive current density (i_{pass}) and critical current density for passivation (i_{crit}) were determined from the polarization curves and are displayed in Table 4. The values of i_{pass} were determined as the current densities corresponding to 0.4 $V_{Ag/AgCl}$, a potential in the most stable part of the passive region for all samples.

The potentiodynamic polarization curves present well-defined passivity with a clear active-passive transition. All conditions displayed a critical current density for passivation (i_{crit}). The 15′-film is more easily passivated as indicated by its low i_{crit} when compared to the 30′ condition. The passive current densities of the coated substrate are lower than that of the uncoated material. This parameter controls surface anodic dissolution, being regarded as a measure of its corrosion resistance under the experimental conditions employed in the present work. In this respect, the data shown in Table 4 confirm the feasibility of using Nb_2O_5 to improve the corrosion properties of the 316 substrate in the PEMFC simulated environment, confirming the EIS results. The Flade potential was more cathodic for the coated material with respect to the uncoated substrate, also pointing to an easier passivation process after Nb_2O_5 deposition. Transpassive dissolution starts at similar potentials for all samples. By considering the horizontal lines, marking the typical anode and cathode operating potentials of PEMFCs, it is noteworthy that both of them intercept the polarization curves in their anodic parts, independently of the surface condition. Moreover, the current densities are lower for the coated samples when compared to the uncoated substrate. The anodic currents of the 15′-film are the lowest at −0.1 $V_{Ag/AgCl}$ and 0.6 $V_{Ag/AgCl}$, confirming its good corrosion properties.

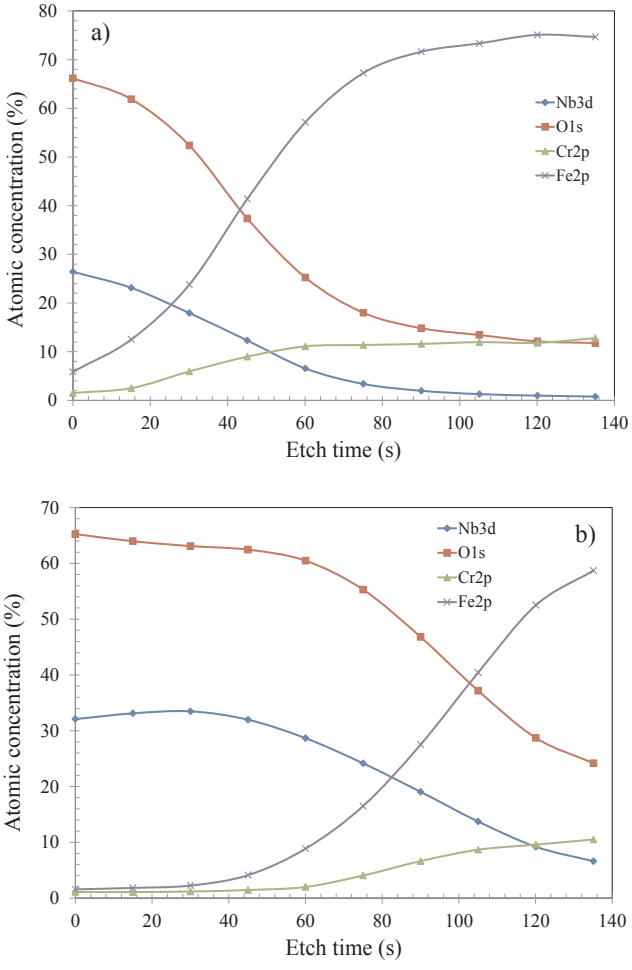

Fig. 4. Variation of the atomic concentrations of Nb3d, O1s, Fe2p and Cr2p with the etch time for the different niobium-based films: (a) 15 min; (b) 30 min.

Potentiostatic polarization curves of the uncoated and Nb_2O_5-coated AISI 316 stainless steel immersed in 0.5 M H_2SO_4 + 2 ppm HF solution at room temperature were obtained at −0.1 $V_{Ag/AgCl}$ and 0.6 $V_{Ag/AgCl}$. The current densities were monitored for 1 h. The results are shown in Fig. 8. All current densities are positive, independently of the applied potential. This behavior was expected, since the corrosion potentials

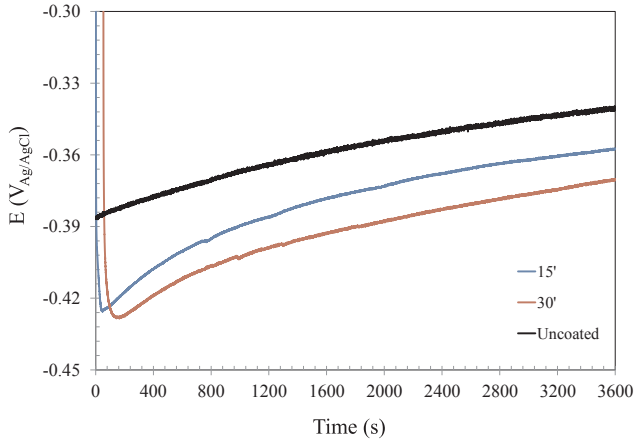

Fig. 5. Open circuit potential versus time for the uncoated and Nb_2O_5-coated AISI 316 stainless steel upon immersed in 0.5 M H_2SO_4 + 2 ppm HF solution at room temperature.

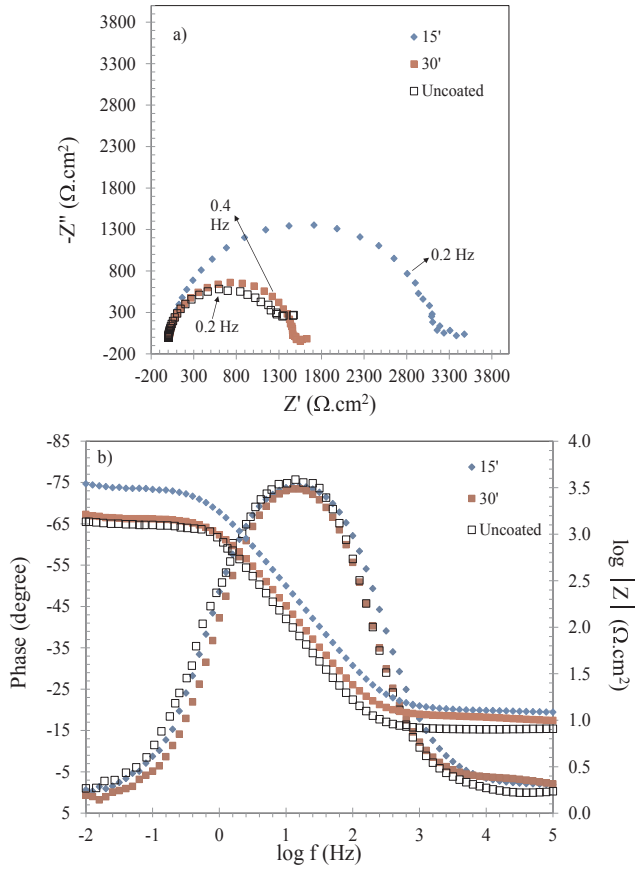

Fig. 6. (a) Nyquist and (b) Bode plots for the uncoated and Nb_2O_5-coated AISI 316 stainless steel specimens in 0.5 M H_2SO_4 + 2 ppm HF solution at room temperature.

observed in Fig. 7 are more negative than −0.1 $V_{Ag/AgCl}$ for all samples, corresponding to the anodic part of the polarization curves.

The current densities at −0.1 $V_{Ag/AgCl}$ (Fig. 8a) are higher than at +0.6 $V_{Ag/AgCl}$ (Fig. 8b) for the same surface condition. This result is in agreement with the potentiodynamic polarization curves shown in Fig. 7, indicating that anodic dissolution is faster at the typical anode PEMFC operating potential. The lowest current densities were observed for the 15′-film either at −0.1 or 0.6 $V_{Ag/AgCl}$, revealing that its corrosion kinetics is the slowest one at both potentials.

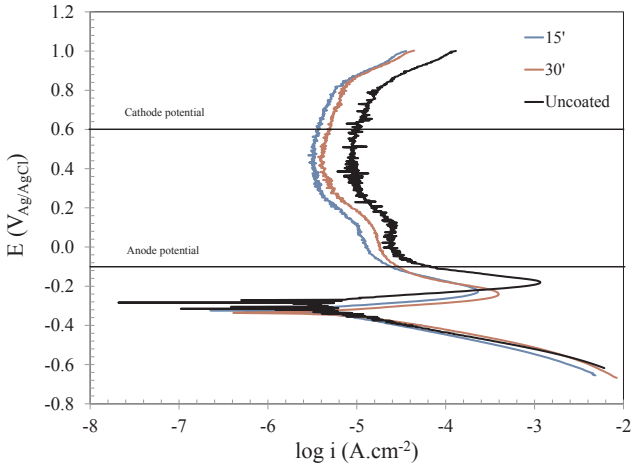

Fig. 7. Potentiodynamic polarization curves for the uncoated and Nb_2O_5-coated AISI 316 stainless steel upon immersed in 0.5 M H_2SO_4 + 2 ppm HF solution at room temperature.

Table 4
Electrochemical parameters determined from the potentiodynamic polarization curves shown in Fig. 7.

	E_{corr} ($mV_{Ag/AgCl}$)	E_{Flade} ($mV_{Ag/AgCl}$)	i_{pass} ($\mu A \cdot cm^{-2}$)	i_{crit} ($mA \cdot cm^{-2}$)
Uncoated	−284	−179	9.62	1.15
15′	−323	−218	3.16	0.22
30′	−336	−238	4.17	0.40

4. Discussion

As shown in the previous section the 15′-film displays the highest corrosion resistance in the 0.5 M H_2SO_4 + 2 ppm HF solution in spite of being thinner than the 30′-film. Although film thickness is an important feature for the barrier effect of protective coatings, other factors can have a more prominent influence on the corrosion protection efficiency. Film porosity is one of them. In a previous work [27], our group has shown that Nb_2O_5 films obtained in similar conditions to those employed in the present work were more effective against corrosion when deposited at 15′ than at 30′, in spite of the thicker layer obtained for the longest deposition time. Film porosity increased with the deposition time, giving rise to the lower corrosion resistance of the 30′-film.

In addition to coating thickness and compactness, surface chemistry has a remarkable influence on the corrosion protection ability of thin films. The high chemical stability of the 15′-film when compared to the 30′-film can also arise from its different surface chemical states. In fact, according to the XPS high resolution spectra (Section 3.1.2), the main components of both films in the Nb3d region were Nb_2O_5 and NbO_2, showing a mixture of the Nb^{5+} and Nb^{4+} oxidation states. As the deposition time increased from 15 to 30 min, the film became enriched in Nb^{4+} and the Nb^{5+}/Nb^{4+} ratio decreased, as shown in Table 2.

The explanation for the enrichment of the niobium-based film with the lower oxidized Nb^{4+} state as the deposition time increased from 15 to 30 min can be hypothesized by further evaluating the XPS depth profile of Nb3d, Fe2p and Cr2p core levels. In Fig. 9 the evolution of the XPS high resolution spectra with the sputtering time is presented for the 15′-film. It is seen that for the Nb3d core level (Fig. 9a) one additional component appears after etching the film surface for 45 s. As the sputtering time increases the atomic concentration of Nb3d decreases, as shown in Fig. 4a and its signal becomes weak. This can be perceived for the spectra obtained at an etch time of 135 s in Fig. 9a. In spite of this relatively weak signal, deconvolution of the Nb3d spectra provided evidence for the presence of Nb^{2+} species in the 15′-film after etching

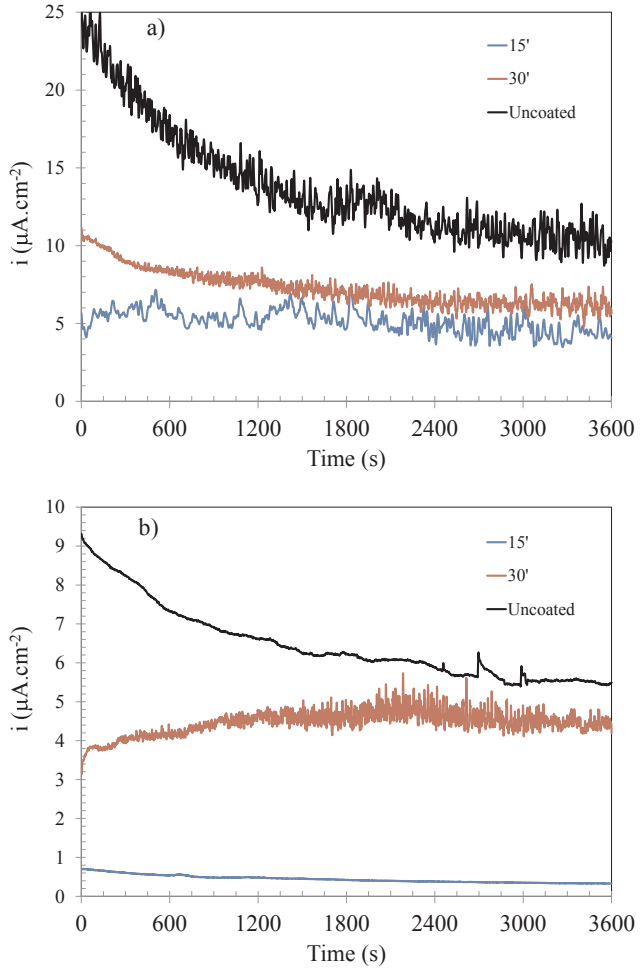

Fig. 8. Potentiostatic polarization curves for the uncoated and Nb_2O_5-coated AISI 316 stainless steel upon immersed in 0.5 M H_2SO_4 + 2 ppm HF solution at room temperature: (a) Polarization at −0.1 $V_{Ag/AgCl}$; (b) Polarization at +0.6 $V_{Ag/AgCl}$.

for 45 s in addition to Nb^{5+} and Nb^{4+}. One example of one Nb3d fitted spectrum is shown in Fig. 10a for the etch time of 75 s. The film consisted of a mixture of Nb^{5+}, Nb^{4+} and Nb^{2+}. In this respect, the film contains Nb_2O_5 as the main component and also NbO_2 and NbO. The binding energies associated with each component are in good agreement with the literature [30,42]. The same trend was observed for longer etching times (fitted spectra not presented).

Yet, it is clearly seen from Fig. 9b and c that Fe2p and Cr2p signals are detected in the film surface even at the beginning of the experiment (0 s) and these signals increase and become more clearly resolved as the etching time increases. The removal of top layers by sputtering the film surface with argon ions during depth profile experiments led to an increase of both iron and chromium atomic concentrations as previously shown in Fig. 4a. The XPS spectra for Fe2p and Cr2p core levels were deconvoluted. One example is shown in Fig. 10b and c for the etch time of 75 s. The fitted spectra revealed that the components for the Fe2p core level are metallic iron (Fe0), FeO, Fe_2O_3, FeOOH and one weak satellite for the Fe^{2+} state. These results are in agreement with data published by other authors [43–45]. The components for the Cr2p core level were metallic chromium (Cr^0), Cr_2O_3 and $Cr(OH)_3$. The binding energies associated with these components are also in good agreement with the literature [46,47]. The same components were observed for the spectra obtained at the other etching times and the fitted spectra are not shown here.

The main differences observed for the spectra obtained during the

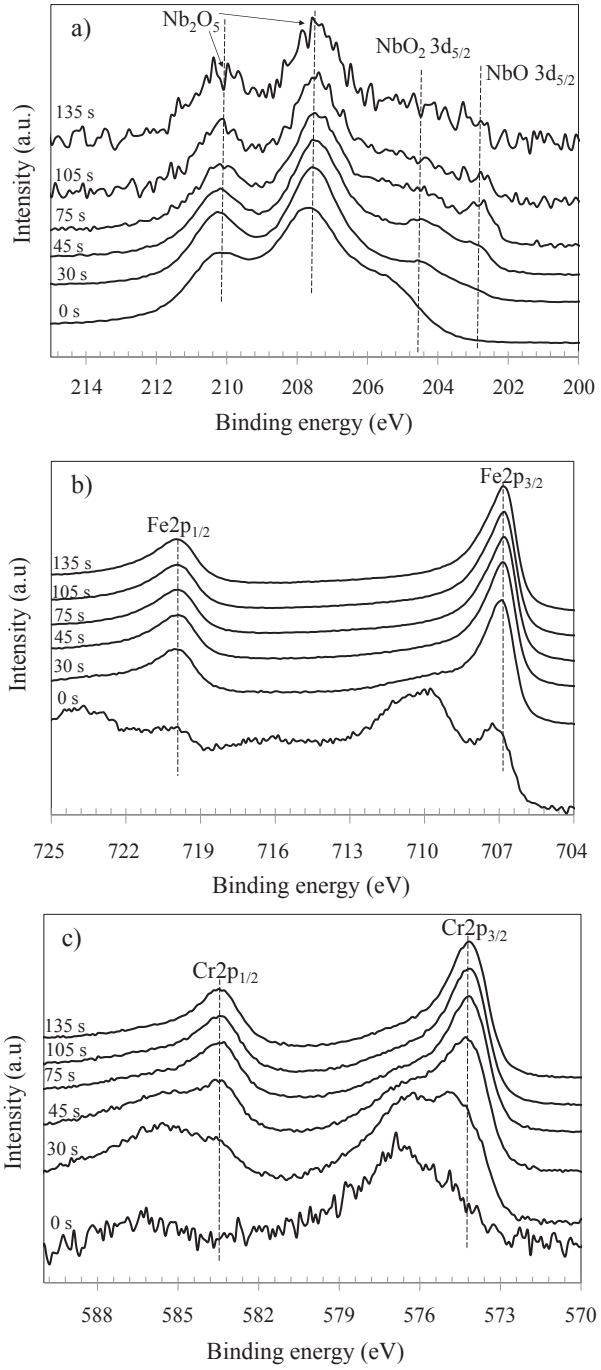

Fig. 9. Evolution of the XPS high resolution spectra with the sputtering time for the 15′-film: (a) Cr2p; (b) Fe2p and (c) Nb3d core levels.

depth profile experiment performed with the 30′-film are regarded to the atomic concentrations of the main elements on the film surface, as outlined in Section 3.1 (Fig. 4b). The Nb3d signal is stronger at the end of the depth profile experiment (Fig. 11a) as the film thickness is higher for this condition when compared to the 15′-film. Notwithstanding, the same components were observed when the spectra were deconvoluted. The film is comprised of a mixture of Nb_2O_5, NbO_2 and NbO at the inner layers whereas NbO is absent at the top layers, as also observed for the 15′-film (Fig. 9a).

The signals for Fe2p and Cr2p are weaker at the beginning of the sputtering cycles when compared with those obtained for the 15′-film (Fig. 11b and c). As the etch time increases these signals become stronger and the typical spin-orbit splitting of Cr2p and Fe2p core levels

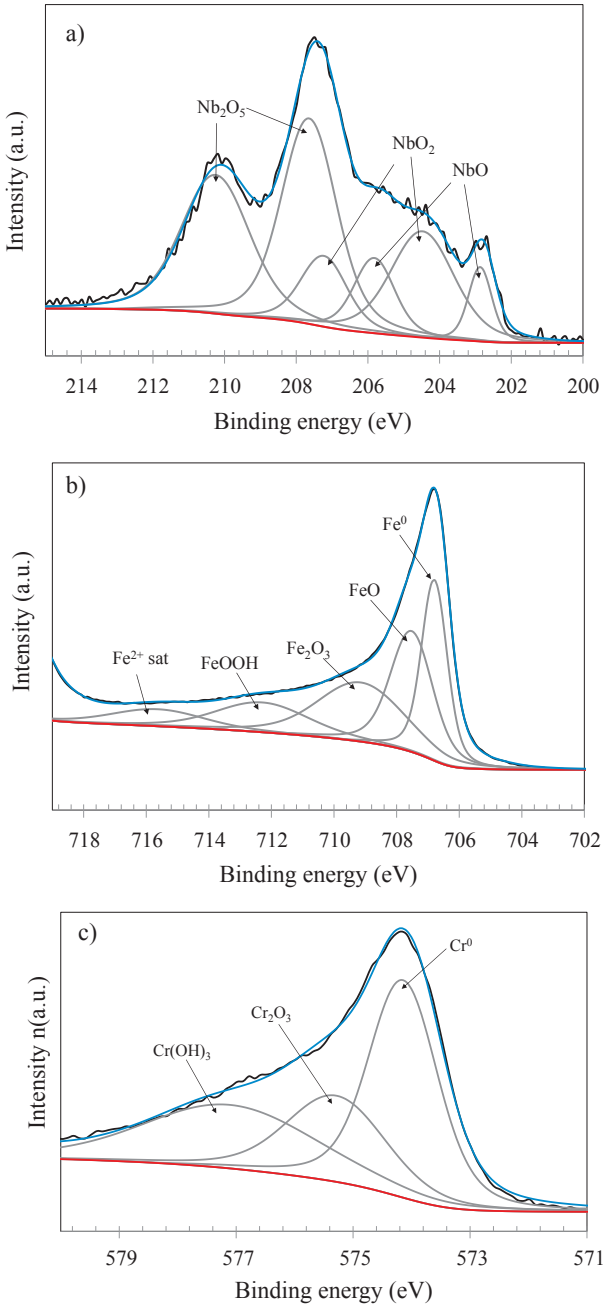

Fig. 10. XPS high resolution spectra for the 15′-film after 75 s sputtering: (a) Nb3d; (b) Fe2p$_{3/2}$ and (c) Cr2p$_{3/2}$.

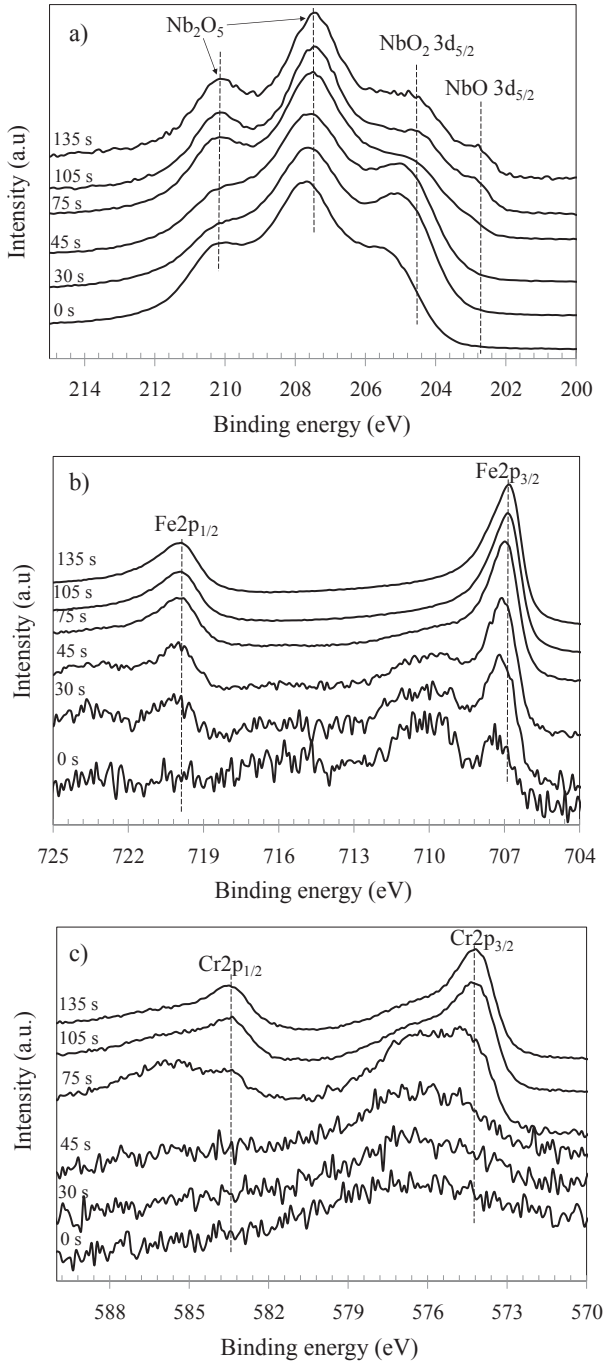

Fig. 11. Evolution of the XPS high resolution spectra with the sputtering time for the 30′-film: (a) Cr2p; (b) Fe2p and (c) Nb3d core levels.

can be clearly seen. The Fe2p and Cr2p spectra obtained for the 30′-film were deconvoluted and the same components obtained for the 15′-film were observed. In this respect, the fitted spectra are not presented here, since they are very similar to those obtained for the 15′-film (Fig. 10).

The scenario depicted above unequivocally shows the presence of iron and chromium concomitantly with niobium species in the niobium-based films even prior to etching by argon ions irrespective of the deposition time. The formation of the less oxidized Nb^{4+} and Nb^{2+} species in niobium oxide films is associated with oxygen deficiency during deposition. In our case, it is possible that oxygen molecules combined with iron and chromium atoms from the steel substrate during deposition, giving rise to the formation of the less stable NbO and NbO_2 species in addition to Nb_2O_5 due to the oxygen deficiency during the PVD process. This effect would be more intense at the beginning of the deposition process so that NbO is only encountered at inner layers due to the more prompt availability of iron and chromium atoms from the substrate. The top surface, in turn, contains only Nb_2O_5 and NbO_2 as the film becomes thicker and the reaction of oxygen molecules with atoms from the substrate becomes more difficult. Thus, NbO does not form.

A consequence of such mechanism would be the decrease of the ratio Nb^{5+}/Nb^{4+} in the film as the deposition time increases from 15 to 30 min, as shown in Table 2. In spite of the inherent uncertainty in the quantitative evaluation of XPS data [48], the results shown in Figs. 9 and 11 reveal the presence of iron and chromium in the films at all etch times. These elements, by combining with oxygen molecules during deposition, would decrease the availability of oxygen molecules to combine with niobium, giving rise to different niobium oxide species such as Nb_2O_5, NbO_2 and NbO, instead of pure Nb_2O_5. This effect would

be enhanced for longer deposition times, increasing the concentration of Nb^{4+} in the film, thus leading to a reduction of the Nb^{5+}/Nb^{4+} ratio. According to Ramírez et al. [49] the O_2 amount in the deposition chamber affects the type of niobium oxide obtained during PVD process. Moreover, the exact amount needed to produce specific oxide species may vary from system to system and it is not a known parameter. Our work points that the interaction of oxygen molecules with atoms from the substrate can affect the composition of the niobium oxide film. Even though this effect have not led to remarkable differences of the atomic concentrations of the oxide species on the film surfaces, it was sufficient to affect the film protective character against corrosion.

The more insulating character of Nb_2O_5 with respect to the more conducting character of NbO_2 has been reported in the literature [50]. The lower reactivity of the 15′-film arises from its Nb_2O_5 enriched surface that enhances its corrosion resistance. In addition to this, Nb_2O_5 has been reported to be strongly adherent and protective [51]. The favorable surface chemistry coupled to the more compact film structure would enhance the stability of the niobium-based films in 0.5 M H_2SO_4 + 2 ppm HF solution. In this respect, the corrosion properties of such films can be tailored in order to improve its chemical stability, allowing the development of optimized layers to withstand the acidic environment of PEM fuel cells.

5. Conclusions

Nb_2O_5 thin films were obtained by magnetron sputtering on AISI 316 stainless steel specimens. The deposition times were 15 and 30 min. The surface chemistry of the sputtered layers was affected by the deposition time. Although both films presented a mixture of Nb^{5+} and Nb^{4+} oxidation states, the film obtained at 15 min presented higher Nb^{5+}/Nb^{4+} ratio. The corrosion behavior of the 316-coated specimens was influenced by the surface chemistry. The corrosion current densities and anodic current densities were lower for the 15′-film and impedance values were higher. Surface enrichment in the low reactivity Nb^{5+}-species was correlated with the superior corrosion properties of the 15′-film. The performance of the niobium-based films against corrosion can be tailored during magnetron sputtering by controlling the deposition time.

Acknowledgments

Authors are thankful to CBMM (Brazil) for kindly providing the niobium target for the deposition process.

References

[1] K. Nikolov, K. Bunk, A. Jung, J.W. Gerlach, P. Kaestner, C.-P. Klages, Combined plasma surface modification of austenitic stainless steel for bipolar plates, Surf. Coat. Technol. 328 (2017) 142–151.
[2] Y. Yu, S. Shironita, T. Mizukami, K. Nakatsuyama, K. Souma, M. Umeda, Corrosion-resistant characteristics of nitrided Ni-free stainless steel for bipolar plate of polymer electrolyte fuel cell, Int. J. Hydrogen Energy 42 (2017) 6303–6309.
[3] M.C.L. De Oliveira, G. Ett, R.A. Antunes, Materials selection for bipolar plates for polymer electrolyte membrane fuel cells using the Ashby approach, J. Power Sources 206 (2012) 3–13.
[4] N.F. Asri, T. Husaini, A.B. Sulong, E.H. Majian, W.R.W. Daud, Coating of stainless steel and titanium bipolar plates for anticorrosion in PEMFC: a review, Int. J. Hydrogen Energy 42 (2017) 9135–9148.
[5] E.F. Mine, Y. Ito, Y. Teranishi, M. Sato, T. Shimizu, Surface coating and texturing on stainless steel plates to decrease the contact resistance by using screen printing, Int. J. Hydrogen Energy 42 (2017) 20224–20229.
[6] K. Kin, X. Li, H. Dong, S. Du, Y. Lu, X. Ji, D. Gu, Surface modification of 316 stainless steel with platinum for the application of bipolar plates in high performance proton exchange membrane fuel cells, Int. J. Hydrogen Energy 42 (2017) 2338–2348.
[7] S.-H. Lee, S.-P. Woo, N. Kakati, Y.-N. Lee, Y.-S. Yoon, Corrosion and electrical properties of carbon/ceramic multilayer coated on stainless steel bipolar plates, Surf. Coat. Technol. 303A (2016) 162–169.
[8] M. Wu, C. Lu, T. Hong, G. Chen, D. Wen, H. Zhang, D. Zhang, A. Wang, Chromium interlayer amorphous carbon film for 304 stainless steel bipolar plate of proton exchange membrane fuel cell, Surf. Coat. Technol. 307A (2016) 374–381.
[9] H.-C. Wang, H.-H. Sheu, C.-E. Lu, K.-H. Hou, M.-D. Ger, Preparation of corrosion-resistant and conductive trivalent Cr-C coatings on 304 stainless steel for use as bipolar plates in proton exchange membrane fuel cells by electrodeposition, J. Power Sources 293 (2015) 475–483.
[10] R. Taherian, A review of composite and metallic bipolar plates in proton exchange membrane fuel cell: materials, fabrication, and material selection, J. Power Sources 265 (2014) 370–390.
[11] L. Wang, J. Sun, B. Kang, S. Li, S. Ji, Z. Wen, X. Wang, Electrochemical behavior and surface conductivity of niobium carbide-modified austenitic stainless steel bipolar plate, J. Power Sources 246 (2014) 775–782.
[12] M. Zhang, G. Lin, B. Wu, Z. Shao, Composition optimization of arc ion plated CrN_x films on 316L stainless steel as bipolar plates for polymer electrolyte membrane fuel cells, J. Power Sources 205 (2012) 318–323.
[13] M. Alishahi, F. Mahboudi, S.M.M. Khoie, M. Aparício, R. Hübner, F. Soldera, R. Gago, Electrochemical behavior of nanocrystalline Ta/TaN multilayer on 316L stainless steel: novel bipolar plates for proton exchange membrane fuel cells, J. Power Sources 322 (2016) 1–9.
[14] M. Omrani, M. Habibi, M.S.M. Birjandi, Enhanced electrical conductivity of two layers AlN-TiN coating on SS316L as bipolar plate using plasma focus device, Int. J. Hydrogen Energy 41 (2016) 5028–5036.
[15] F. Bi, L. Peng, P. Yi, X. Lai, Multilayered Zr-C/a-C film on stainless steel 316L as bipolar plates for proton exchange membrane fuel cells, J. Power Sources 314 (2016) 58–65.
[16] Y. Zhao, L. Wei, P. Yi, L. Peng, Influence of Cr-C film composition on electrical and corrosion properties of 316L stainless steel as bipolar plates for PEMFCs, Int. J. Hydrogen Energy 41 (2016) 1142–1150.
[17] P. Lettenmeier, R. Wang, R. Abouatallah, B. Saruhan, O. Freitag, P. Gazdzicki, T. Morawietz, R. Hiesgen, A.S. Gago, K.A. Friedrich, Low-cost and durable bipolar plates for proton exchange membrane electrolyzers, Sci. Rep. 7 (2017) 44035.
[18] F.B. Destro, M. Cilense, M.P. Nascimento, F.G. García, L.R.O. Hein, A.Z. Simões, Corrosion behaviour of polycrystalline Nb_2O_5 thin films and its size effects, Prot. Met. Phys. Chem. Surf. 52 (2016) 104–110.
[19] E.-B. Liu, X.-F. Cui, G. Jin, Q.-F. Li, T.-M. Shao, Effect of niobium film on corrosion resistance of AZ91D magnesium alloy, Key Eng. Mater. 525–526 (2013) 9–12.
[20] M.D. Anderson, B. Aitchison, D.C. Johnson, Corrosion resistance of atomic layer deposition-generated amorphous thin films, Appl. Mater. Interfaces 8 (2016) 30644–30648.
[21] P.N. Rojas, S.E. Rodil, Corrosion behavior of amorphous niobium oxide coatings, Int. J. Electrochem. Sci. 7 (2012) 1443–1458.
[22] D. Velten, E. Eisenbarth, N. Schanne, J. Breme, Biocompatible Nb_2O_5 thin films prepared by means of the sol–gel process, J. Mater. Sci. - Mater. Med. 15 (2004) 457–461.
[23] K.T. Jacob, C. Shekhar, M. Vinay, Thermodynamic properties of niobium oxides, J. Chem. Eng. Data 55 (2010) 4854–4863.
[24] P. Amaravathy, S. Sowndarya, S. Sathyanarayanan, N. Rajendran, Novel sol gel coating of Nb_2O_5 on magnesium alloy for biomedical applications, Surf. Coat. Technol. 244 (2014) 131–141.
[25] M. Mazur, M. Szymanska, D. Kaczmarek, M. Kalisz, D. Wojcieszak, J. Domaradzki, F. Placido, Determination of optical and mechanical properties of Nb_2O_5 thin films for solar cells applications, Appl. Surf. Sci. 301 (2014) 63–69.
[26] G. Ramírez, S.E. Rodil, H. Arzate, S. Muhl, J.J. Olaya, Niobium based coatings for dental implants, Appl. Surf. Sci. 257 (2011) 2555–2559.
[27] M.F. Pillis, G.A. Geribola, G. Scheidt, E.G. de Araújo, M.C.L. de Oliveira, R.A. Antunes, Corrosion of thin, magnetron sputtered Nb_2O_5 films, Corros. Sci. 102 (2016) 317–325.
[28] T.J. Pan, Y. Chen, B. Zhang, J. Hu, C. Li, Corrosion behavior of niobium coated 304 stainless steel in acid solution, Appl. Surf. Sci. 369 (2016) 320–325.
[29] C. Cao, C. Liang, N. Huang, Electrochemical behavior of niobium electrodeposited 316 stainless steel bipolar plate for PEMFC in choline chloride based ionic liquids, J. Wuhan Univ. Technol. Mater. Sci. Ed. 30 (2015) 1061–1067.
[30] J.J. Si, X.H. Chen, Y.H. Cai, Y.D. Wu, T. Wang, X.H. Hui, Corrosion behavior of Cr-based bulk metallic glasses in hydrochloric acid solutions, Corros. Sci. 107 (2016) 123–132.
[31] K. Feng, Z. Li, Y. Cai, P.K. Chu, Corrosion behavior and electrical conductivity of niobium implanted 316L stainless steel used as bipolar plates in polymer electrolyte membrane fuel cells, Surf. Coat. Technol. 205 (2010) 85–94.
[32] T. Choso, M. Kamada, K. Tabata, The effects of heat treatments upon NO adsorption for a single Crystal of $LiNbO_3$, Appl. Surf. Sci. 121–122 (1997) 387–390.
[33] K. Tabata, T. Choso, Y. Nagasawa, The topmost structure of annealed single Crystal of $LiNbO_3$, Surf. Sci. 408 (1998) 137–145.
[34] S. Li, C.N. Schmidt, Q. Xu, X. Cao, G. Cao, Macroporous nanostructured Nb_2O_5 with surface Nb^{4+} for enhanced lithium ion storage properties, Chem. Nanomat. Energy Biol More 2 (2016) 675–680.
[35] A. Kawashima, S. Watanabe, K. Asumi, S. Hamada, XPS study of corrosion behavior of Ti-18Nb-4Sn shape memory alloy in a 0.05 mass% HCl solution, Mater. Trans. 44 (2003) 1405–1411.
[36] H. Luo, X. Wang, C. Dong, K. Xiao, X. Li, Effect of cold deformation on the corrosion behaviour of UNS S31803 duplex stainless steel in simulated concrete pore solution, Corros. Sci. 124 (2017) 178–192.
[37] L. Franta, J. Fojt, L. Joska, J. Kronek, L. Cvrcek, J. Vyskocil, Z. Cejka, Hinge-type knee prosthesis wear tests with a mechanical load and corrosion properties monitoring, Tribol. Int. 63 (2013) 61–65.
[38] B.M. Fernández-Pérez, J.A. González-Guzmán, S. González, R.M. Souto, Electrochemical impedance spectroscopy investigation of the corrosion resistance of a waterborne acrylic coating containing active electrochemical pigments for the

protection of carbon steel, Int. J. Electrochem. Sci. 9 (2014) 2067–2079.
[39] W. Liu, S.-L. Lu, Y. Zhang, Z.-C. Fang, X.-M. Wang, M.-X. Lu, Corrosion performance of 3%Cr steel in CO_2-H_2S environment compared with carbon steel, Mater. Corros. 66 (2015) 1232–1244.
[40] C. Li, Y. Ma, Y. Li, F. Wang, EIS monitoring study of atmospheric corrosion under variable relative humidity, Corros. Sci. 52 (2010) 3677–3686.
[41] S. Shreepathi, P. Bajaj, B.P. Mallik, Electrochemical impedance spectroscopy investigations of epoxy zinc rich coatings: Role of Zn content on corrosion protection mechanism, Electrochim. Acta 55 (2010) 5129–5134.
[42] K. Kowalski, A. Bernasik, W. Singer, J. Camra, In situ XPS investigation of the baking effect on the surface oxide structure formed on niobium sheets used for superconducting RF cavity production, in: Proceedings of the 11th Workshop on RF Superconductivity, Lübeck/Travemünder, Germany, 2003.
[43] A. Kocijan, C. Donik, M. Jenko, Electrochemical and XPS studies of the passive film formed on stainless steels in borate buffer and chloride solutions, Corros. Sci. 49 (2007) 2083–2098.
[44] H. Luo, X. Wang, C. Dong, K. Xiao, X. Li, Effect of cold deformation on the corrosion behavior of UNS S31803 duplex stainless steel in simulated pore solution, Corros. Sci. 124 (2017) 178–192.
[45] H. Xu, L. Wang, D. Sun, H. Yu, The passive oxide films growth on 316L stainless steel in borate buffer solution measured by real-time spectroscopic ellipsometry, Appl. Surf. Sci. 351 (2015) 367–373.
[46] J. Lv, M. Yang, M. Hideo, T. Liang, The effect of surface enriched chromium and grain refinement by ball milling on corrosion resistance of 316L stainless steel, Mater. Res. Bul. 91 (2017) 91–97.
[47] S. Habibzadeh, L. Li, D. Shum-Tim, E.C. Davis, S. Omanovic, Electrochemical polishing as a 316L stainless steel surface treatment method: Towards the improvement of biocompatibility, Corros. Sci. 87 (2014) 89–100.
[48] S. Tougaard, Surface nanostructure determination by X-ray phoemission spectroscopy peak shape analysis, J. Vac. Sci. Technol. A 14 (1996) 1415–1423.
[49] G. Ramírez, S.E. Rodil, S. Muhl, D. Turcio-Ortega, J.J. Olaya, M. Rivera, E. Camps, L. Escobar-Alarcón, Amorphous niobium oxide thin films, J. Non-Cryst. Solids 356 (2010) 2714–2721.
[50] K. Senevirathne, R. Hui, S. Campbell, S. Ye, J. Zhang, Electrocatalytic activity and durability of Pt/NbO_2 and Pt/Ti_4O_7 nanofibers for PEM fuel cell oxygen reduction reaction, Electrochim. Acta 59 (2012) 538–547.
[51] C.S. Brandolt, J.G. de Souza Junior, S.R. Kunst, M.R.O. Vega, R.M. Schroeder, C.F. Malfatti, Mater. Res. 17 (2014) 866–877.